International Journal of Computer Vision 31(2/3), 129–144 (1999)

Bidirectional Reflection Distribution Function of Thoroughly Pitted Surfaces

JAN J. KOENDERINK AND ANDREA J. VAN DOORN
Helmholtz Instituut, Universiteit Utrecht, Buys Ballot Laboratory, Princetonplein 5,3584CC Utrecht, The Netherlands
j.j.koenderink@phys.uu.nl

KRISTIN J. DANA AND SHREE NAYAR
Department of Computer Science, Columbia University, New York, NY 10027
nayar@cs.columbia.edu

Abstract. We derive the BRDF (Bidirectional Reflection Distribution Function) at the mega scale of opaque surfaces that are rough on the macro and micro scale. The roughness at the micro scale is modeled as a uniform, isotropically scattering, Lambertian surface. At the macro scale the roughness is modeled by way of a distribution of spherical concavities. These pits influence the BRDF via vignetting, cast shadow, interreflection and interposition, causing it to differ markedly from Lambertian. Pitted surfaces show strong backward scattering (so called "opposition effect"). When we assume that the macro scale can be resolved, the radiance histogram and the spatial structure of the textons of the textured surface (at the mega scale) can be calculated. This is the main advantage of the model over previous ones: One can do exact (numerical) calculations for a surface geometry that is physically realizable.

Keywords: bidirectional reflection distribution function, photometry, surface scattering, texture, physical properties

1. Introduction

1.1. The problem

Most surfaces encountered in the natural environment are quite different from those commonly encountered in the optics laboratory, that is to say, smoothly polished transparent dielectrics (glass) or metals (silver or aluminum mirror coatings) deposited on smooth surfaces (Longhurst 1957). Many naturally occurring surfaces are boundaries of opaque, often inhomogeneous bulk materials (*e.g.*, wood, granite, paper, cloth, bread, ...) with a geometrically articulated ("rough") surface (Gibson 1950, Hunter 1975). Although the reflection/refraction of beams of radiation by almost all surfaces (we have to exclude true "fractal" surfaces with structure down to the sub–wavelength scale here) is well described by the Fresnel equations (Born and Wolf 1980) on the *micro scale*, this description is essentially useless on the macro or mega scale. The surface remission of many so called "matte" surfaces is approximately captured by "Lambert's Law" (Lambert 1760, Kortüm 1969): The radiance of the remitted beam is *independent* of the viewing direction and depends only on the irradiance. Such surfaces scatter the incident radiation "completely" in the sense that the directional remittance gives no clue as to their material or geometrical make up. Lambert's "Law" is not to be understood in a mechanistic sense, it is simply the constant term in a series development of the dependence of the

scattered radiance on the directions of the incident and scattered beams. In reality all real surfaces deviate to some extent from this conceptually simplest model (Kortüm 1969), thus (partly) revealing their nature in remote sensing. One may conceive of Lambertian scattering as due to roughness on the micro scale, a scale that is not resolved by the observer (Beckmann and Spizzichino 1963, Kerker 1969). When the scattered radiation has been thoroughly scrambled through multiple scattering the surface may approach the Lambertian limit, in fact many natural surfaces (chalk, blotting paper) come close. Deviations from Lambert's Law may derive from many effects, the most common being shadowing (rough plaster) and regular reflection/refraction (glazed porcellain).

A great many natural surfaces are rough on *multiple scales* (see figure 1). The surface on the (unresolved) micro scale can often be approximated by the Lambertian model, but additional roughness on what we call the macro scale checks the average remittance on the mega scale (the mega scale disregards the surface articulations on the macro scale). The macro scale articulations lead to local photometrical and geometrical effects like cast shadows, interreflections and interposition, thus inducing local fluctuations of the remitted radiance. We will treat such fluctuations as *texture*. The overall remittance is an average over these textural variations, whereas the fluctuations show up in the shape of the radiance histogram and in the spatial structure of the radiance variations. For instance, a rough plaster on a wall can be said to remit a certain percentage of the incident radiation *on the average* (its "albedo" on the mega scale) but also displays variations of the radiance (the visible "texture") which shows up in the radiance histogram. On the microscale the plaster is roughly Lambertian (scatters in all directions) due to a random packing of transparent calciumcarbonate crystals on a "nano scale" (sub–micro scale).

Such rough surfaces are very common indeed, and their photometrical properties are quite distinct from those associated with the Lambertian surface. Although *ad hoc* phenomenological models are quite common (especially in computer graphics rendering (Blinn 1977, Foley *et al* 1990)), it is obviously preferable to develop realistic models that reflect the relevant physics. One advantage of such models is that the model can also predict texture and radiance histograms as a function of viewing and irradiation geometry. The common technique of "texture mapping"

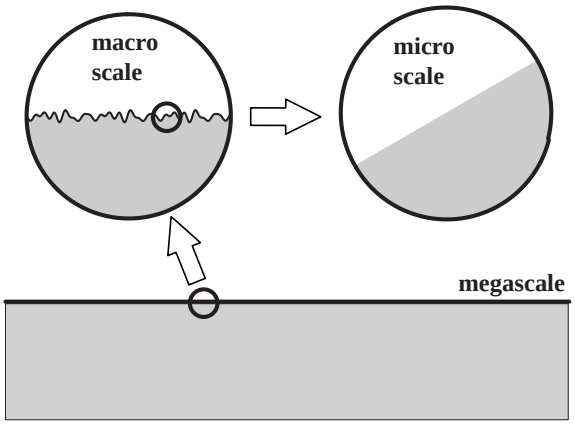

Fig. 1. Surface at various scales. At the mega scale the surface is flat, at the macro scale it is articulated. The articulations cause vignetting, cast shadow and interreflection. At the micro scale the surface is considered flat again, though the surface normal may deviate from that at the mega scale. At the micro scale the surface is assumed to scatter radiation in the Lambertian fashion: Of course this implies roughness at a still finer scale ("nano scale, not illustrated).

(Foley *et al* 1990) may be fast, but it is unsatisfactory in many cases because leading to unrealistic results and lacking conceptual foundation.

1.2. Major radiometric and geometrical effects

When we assume the surface to be opaque and scattering radiation on a micro scale via some given bidirectional (directions of incident and remitted beams) scattering function, there are essentially only four radiometric and geometrical effects to consider:
—*Interposition* is a geometrical effect that causes certain parts of the surface to be invisible from a given viewing position because occluded by other parts of the surface. Such an effect is well known from our experiences in a hilly countryside: We often fail to spot objects because they happen to be "behind yonder hill";
—*Vignetting* is a radiometric effect that causes certain parts of the surface to be irradiated only by part of the sources. The reason is essentially interposition: The surface element cannot "see" part of the source because another part of the surface is interposited;
—*Cast shadows* are a result of vignetting. However, because of their conspicuousness we mention them here explicitly;
—*Interreflections* are due to the fact that parts of the surface act as "secondary radiators" for other parts of the surface. Even parts of the surface that are not irra-

diated by the (primary) source at all (and thus would be expected to be in total darkness) might still be irradiated by other (irradiated) parts of the surface. Thus the interreflections capture *multiple scattering* on the macro scale. (Multiple scattering on the *micro* scale is described via the Lambertian property.)

Notice that these effects depend on the *global* structure of the rough surface. For instance, a hill may cast an arbitrarily long shadow on a plane. This makes the problem a very hard one. The conventional treatment of reflection/refraction at a planar interface (the Fresnel equations) is so simple exactly because it is purely *local*.

1.3. The Bidirectional Reflection Distribution Function (BRDF)

In radiometry one simply *adds* contributions from various beams *linearly* because they can be treated as mutually "incoherent" (Born and Wolf 1980): Thus the superposition leads to simple addition (of radiant power spectra). As a consequence we can evaluate the effect of *extended sources* via integration once we know the scattering of *directed* beams (Fock 1924, Gershun 1939, Moon and Spencer 1981). Thus we need only consider incident beams of vanishing angular spread. Because this is really a singular case (beams of vanishing angular spread have zero "throughput" or étendue (Gershun 1939, Moon and Spencer 1981) we will specify the strength of the incident beams in terms of their "normal irradiance", *i.e.*, the irradiance caused by the beam on a surface element placed orthogonal to the beam. Then the direction and normal irradiance completely specify the incident beams and thus the source geometry.

We consider a surface element with (mega scale!) outward surface normal $\mathbf{n}$. Let the incident beam be *from* a direction $\mathbf{i}$. We consider the radiance of a beam scattered in the direction $\mathbf{e}$. Let the vectors $\mathbf{a}$ and $\mathbf{b}$ be a positively oriented, orthonormal basis for the (mega scale) surface. Let $\mathbf{n} = \mathbf{a} \times \mathbf{b}$. We will typically express the incident and exit directions in terms of the basis $\{\mathbf{a}, \mathbf{b}, \mathbf{n}\}$. The incident beam causes an irradiance $H^\perp \mathbf{n} \cdot \mathbf{i}$, where $H^\perp$ denotes the normal irradiance caused by the beam. Let the radiance of the exit beam be $N(\mathbf{e})$, then one defines the "Bidirectional Reflection Distribution Function" or BRDF (Gershun 1939, Moon and Spencer 1981, Nicodemus *et al* 1977) as the ratio of the radiance of the exit beam to the irradiance caused by the incident beam, that is to say

$$\mathrm{BRDF}(\mathbf{i}, \mathbf{e}) = \frac{N(\mathbf{e})}{H^\perp \mathbf{i} \cdot \mathbf{n}}. \tag{1}$$

This is a useful definition because it essentially represents a way of "bookkeeping of rays". Thus we have the fundamental symmetry ("Helmholtz reciprocity", see Minnaert 1941) $\mathrm{BRDF}(\mathbf{i}, \mathbf{e}) = \mathrm{BRDF}(\mathbf{e}, \mathbf{i})$, which merely expresses the fact that—in geometrical optics—rays can be *reversed*, that is to say, if one reverses each single ray in some optical ray field, the reversed field again represents a possible physical situation.

Once the BRDF of a surface is known we can calculate the radiance in arbitrary viewing geometries for arbitrary source geometries (extended sources) via integration.

Notice that for a Lambertian surface the BRDF is a constant (by definition the radiance doesn't depend on the direction of the exit beam). When the *albedo* is ϱ, that is to say, a fraction ϱ of the incident radiation is remitted (the remainder being absorbed by the surface material), conservation of rays enables us to find the BRDF:

$$\mathrm{BRDF}_{\text{Lambertian}}(\mathbf{i}, \mathbf{e}, \varrho) = \frac{\varrho}{\pi}. \tag{2}$$

1.4. Existing models

We confine the discussion to models with a basis in physics (Beckmann and Spizzichino 1963, Kerker 1969, Kortüm 1969, Nayar *et al* 1991, Koenderink and van Doorn 1996), disregarding the purely phenomenological models (such as—among many—Öpik 1924). We limit the discussion to surfaces with a Lambertian BRDF on the micro scale.

Our main interest is a better understanding of the relative contributions of cast shadow, vignetting and interreflection for rough surfaces. Thus we will consider only geometrically and physically realistic models: In this sense the present treatment is primarily of academic interest. From a mere applications oriented perspective the phenomenological methods have much to recommend them. They yield no insight into the essential optics though. Of course a keen insight as to the relative importance of the primary optical effects is a great asset in the formulation of novel phenomenological models.

Models of this type that have been proposed in the literature are the *grooved surface* and the *Gaussian random surface*.

Although the Gaussian random surface is conceptually an important generic case, it suffers from the drawback that no exact solutions are forthcoming. The global nature of the geometrical and radiometrical effects make it virtually impossible to frame anything but approximate statistical models (Beckmann 1965, Smith 1967, Torrance and Sparrow 1967, Wagner 1967, Kerker 1969, Beckmann and Spizzichino 1963). Thus we are stuck with either approximate analytical models or with Monte Carlo simulations. The latter are also important as a check on the various approximations. Approximations that work reasonably well can of course be highly relevant in practice. However, in this paper we restrict ourselves to models that can—at least in principle—be treated with exact methods.

The idea of the grooved surface model is simple and attractive: If the surface articulations are such that the global interactions are at least confined to finite (and known) regions the chances of obtaining an exact solution are much improved. Oren and Nayar (Nayar and Oren 1995, Oren and Nayar 1995) consider concavities in the form of infinitely extended V–grooves. In this case the interactions are confined to the grooves. In particular the treatment of the vignetting (shadowing) becomes rather simple, whereas vignetting presents almost insurmountable difficulties in case of the Gaussian random surface. Interreflections are still complicated and Oren and Nayar treat them only in approximate fashion. However, fair approximations are comparatively easy to find. In order to obtain an isotropic surface Oren and Nayar assume the surface to be covered with V–grooves of infinite extent *in all directions*. This is clearly a geometrical impossibility, thus this model is ill suited to investigate any textural properties. The BRDF for the Oren–Nayar model shows the back scattering characteristic of rough surfaces (rough on the macro scale that is) and has been shown to describe the properties of many realistic surfaces remarkably well. Since these BRDF's are quite distinct from Lambertian (a common assumption), the model— apart from its conceptual value—has important applications in computer vision and graphics rendering.

1.5. The pitted surface model

We propose a "thoroughly pitted surface" model in the following sense: Much of the surface is assumed to be covered (100% is geometrically possible, hence "thoroughly pitted") with *spherical concavities*. The diameter of the concavities is arbitrary (there could be a distribution of sizes) and plays no role for the BRDF. (It *does* play a role for the spatial structure of the texture of course!) The depth to diameter ratio of the concavities is an important parameter, the BRDF depends critically on it. We may assume some distribution of this parameter. Another parameter is the albedo of the Lambertian surface on the micro scale. We consider such a model because:
—Different from the V–groove model, this model is geometrically *possible*. Thus it can be used with confidence to investigate not just the BRDF, but also the radiance histogram and varieties of texture;
—Like the V–groove model (but unlike the Gaussian random surface, see Smith 1967, Wagner 1967) the vignetting can be exactly solved and the result is fairly simple;
—Unlike either the V–groove or the Gaussian random surface, the interreflection problem is very easily (almost trivially) solved in closed form;
—Many natural surfaces can be expected to belong to this general class. The class should be very similar to that covered by the V–groove model.

Notice that the pitted surface model (like the V–groove model) strictly confines the global interactions to a finite region, in this case the interior surfaces of the concavities (Buhl *et al* 1968). This makes these models viable in the first place. In the case of the thoroughly pitted surface this means that we need only treat the case of a *single* concavity: More general cases (distributions of sizes and/or depths) can then be handled via simple averaging.

The pitted surface model has been discussed in the quest for a model of the lunar surface suffiently realistic to explain the photometric "lunation curve". Van Diggelen (1959) gives a convenient review of the literature up to the fifties, with critical discussions and augmented with novel calculations and even model measurements. Earliest models date from the twenties, but van Diggelen stresses Bennet's work of 1938: This theory is well presented in van Diggelen's paper. In this theory interreflections are ignored, and it is assumed that the remitted radiance is proportional to the (projected) irradiated and visible area. (The approximation is thus that the interior surface of the cavity is assumed to be uniformly irradiated.) Van Diggelen quotes the formulas that express the fraction of visible and irradiated area in terms of the angular parameters. Van Diggelen then improves on this (very coarse) approximation by estimating the average irradiance. He

uses an approximation and remarks that the calculations are so complicated that it makes more sense to obtain numerical results through model measurements in the laboratory. These measurements show strong deviations from Lambert's Law, especially a strong back scatter lobe.

2. Radiometric properties of the spherical pit

We will characterize the shape of the cavity (see figure 2) via its "aperture", an angle Ψ such that the diameter of the orifice is $d = 2r = 2R\sin\Psi$, where R denotes the radius of the spherical surface, r the radius of the planar disk of the orifice and the depth $h = R(1-\cos\Psi)$. We will not regard "overhangs", that is to say, the aperture is restricted to the range $\Psi \leq \pi/2$. The deepest pits are thus hemispherical cavities ($\Psi = \pi/2$). For very small apertures the cavities are almost flat, in the limit for zero aperture we obtain the Lambertian surface of the micro scale.

Notice that the surface area of the (planar!) orifice is $\pi r^2 = \pi R^2 \sin^2\Psi$, whereas the area of the surface of the concavity is $4\pi R^2 \sin^2\Psi/2$. Thus the surface area of the hemispherical concavity is twice that of its orifice.

2.1. *Effects of vignetting: Cast shadow and interposition*

The problems of the cast shadow and interposition are very similar: A surface element of the cavity is in shadow if no ("light") ray can reach it and is invisible if no "visual ray" can reach it. Thus we need only discuss one of these cases, the case of the cast shadow say.

It is a matter of simple geometry to see that the edge of the cast shadow is a planar curve, thus a small circle on the spherical surface. Simple symmetry arguments reveal that the radius of this small circle equals that of the orifice of the cavity.

2.2. *Primary irradiation*

For those surface elements of the cavity that don't lie in the cast shadow region the primary irradiance is simply the normal irradiance of the beam times the scalar product of the outward surface normal (at the macro scale!) and the direction from which the beam is arriving. (It is easy to check that the scalar product is invariably non–negative, thus we need not worry about "body shadow". The details are explained in figure 3.)

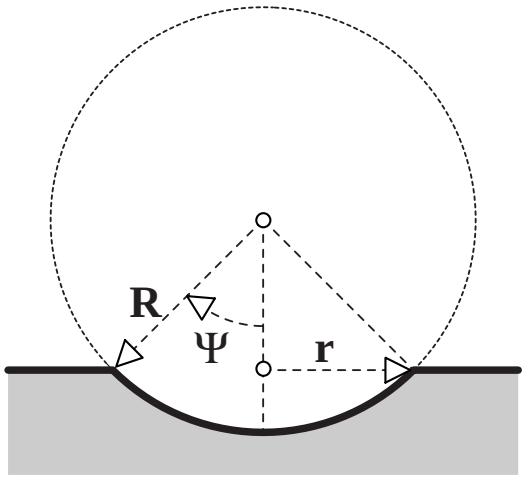

Fig. 2. Parameters of the spherical concavity. The radius of the sphere is R, of the orifice r. The "aperture" of the concavity is characterized by the angle Ψ. We assume $0 \leq \Psi, \leq \pi/2$ throughout, thus avoiding "overhang". For $\Psi = \pi/2$ we have the "hemispherical cavity".

2.3. *Effects of interreflections*

The spherical cavity is an especially convenient case because the interreflection problem can be solved algebraically: In general one has to solve an (often nasty) Fredholm integral equation (Buckley 1927, Moon 1940, Koenderink and van Doorn 1983). The reason is that the étendue of the beam defined by two surface elements on the cavity does not depend on the location of the surface elements at all! In fact, the étendue is (Jacquez and Kuppenheim 1955, Koenderink and van Doorn 1983)

$$\varepsilon(p_1, p_2) = \frac{da_1 da_2}{4R^2}, \tag{3}$$

here (p_1, p_2) are two positions on the surface, (da_1, da_2) infinitesimal surface elements at these positions, and R the radius of the sphere.

The radiance balance equation for the cavity is (Koenderink and van Doorn 1983)

$$H(p) = H^{\text{prim}}(p) + \int_{\text{cavity}} N(q)\frac{1}{4R^2}\, da_q, \tag{4}$$

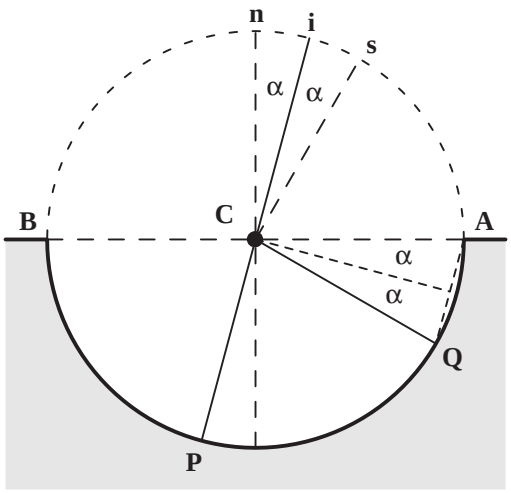

Fig. 3. Geometry of vignetting and the cast shadow. These cases are essentially identical, we discuss the cast shadow here. The incident beam has co–elevation α. The edge of the cast shadow is at Q, which is an angle 2α from the edge of the concavity. The direction **s** is the normal to the plane of the shadow boundary. At P the incident beam impinges normally on the surface of the cavity. The irradiance vanishes on the bisectrix of A and Q which is orthogonal to the direction of incidence. Thus the irradiance is non–negative throughout the part of the cavity BPQ that falls outside the cast shadow region.

here $H(p)$ denotes the irradiance of the surface (in the presence of interreflection) at a generic point p, $H^{\text{prim}}(p)$ the primary irradiance at p (taking only the primary sources into account), and $N(q)$ the radiance (taking interreflections into account) of the beam from the surface element da_q (at q) that throws "secondary irradiation" on the surface at p. Because the surface is assumed Lambertian on the micro scale the radiance is simply related to the irradiance as

$$N(q) = \frac{\varrho H(q)}{\pi}, \tag{5}$$

where ϱ denotes the albedo on the micro scale and we have applied the expression for the BRDF of the Lambertian surface discussed above. Since the albedo is assumed constant we may carry various factors in front of the integral sign and obtain

$$H(p) = H^{\text{prim}}(p) + \frac{\varrho}{4\pi R^2}\int_{\text{cavity}} H(q)\, da_q. \tag{6}$$

We define the average irradiance

$$\langle H\rangle = \frac{1}{4\pi R^2 \sin^2\Psi/2}\int_{\text{cavity}} H(q)\, da_q, \tag{7}$$

where we have used the expression for the surface area of the cavity introduced above.

When we proceed to average the balance equation over the surface of the cavity we obtain

$$\langle H\rangle = \langle H^{\text{prim}}\rangle + \varrho\langle H\rangle \sin^2\Psi/2, \tag{8}$$

an *algebraic* equation instead of the Fredholm integral equation: We may immediately solve for the average radiance:

$$\langle H\rangle = \frac{\langle H^{\text{prim}}\rangle}{1-\varrho\sin^2\Psi/2}. \tag{9}$$

In order to find the average irradiance we need to find the average primary irradiance. The flux that enters the cavity is the irradiance of the plane (at the macro level!) times the area of the orifice. The average primary irradiance is this flux divided by the area of the surface of the cavity. Thus we have

$$\langle H^{\text{prim}}\rangle = \frac{\pi(R\sin\Psi)^2 H^\perp\,\mathbf{n}\cdot\mathbf{i}}{4\pi R^2\sin^2\frac{\Psi}{2}} = \cos^2\frac{\Psi}{2}H^\perp\,\mathbf{n}\cdot\mathbf{i}. \tag{10}$$

Combining results we find an expression for the average irradiance.

Because of the constancy of the mutual étendue for surface elements of the sphere the contribution to the irradiance due to secondary radiation is the same for all surface elements. We call it the "diffuse irradiance" H^{diff}. We have that $H^{\text{diff}} = \langle H^{\text{diff}}\rangle$.The irradiance is thus simply the primary irradiance plus the diffuse irradiance: $H(p) = H^{\text{prim}}(p) + H^{\text{diff}}$. Thus it is easy to find the diffuse irradiance: $H^{\text{diff}} = \langle H\rangle - \langle H^{\text{prim}}(p)\rangle$. We find

$$H^{\text{diff}} = \frac{\varrho\sin^2\Psi}{4(1-\varrho\sin^2\frac{\Psi}{2})}H^\perp\,\mathbf{n}\cdot\mathbf{i}. \tag{11}$$

In the region of the cast shadow the irradiance is just the diffuse irradiance, in the remaining region the irradiance is the sum of the primary irradiance and the diffuse irradiance.

Finally then, the diffuse radiance is

$$N^{\text{diff}} = \frac{\varrho^2\sin^2\Psi}{4\pi(1-\varrho\sin^2\frac{\Psi}{2})}H^\perp\,\mathbf{n}\cdot\mathbf{i}, \tag{12}$$

or, approximately

$$\frac{H^\perp\,\mathbf{n}\cdot\mathbf{i}\sin^2\Psi}{4\pi}\Big(\varrho^2+\varrho^3\sin^2\tfrac{\Psi}{2}+\varrho^4\sin^4\tfrac{\Psi}{2}+\varrho^5\sin^6\tfrac{\Psi}{2}+\varrho^6\sin^8\tfrac{\Psi}{2}+O(\varrho^7)\Big). \tag{13}$$

Notice that a series development with respect to ϱ starts with the quadratic term: This indicates multiple (at least twice) scattering. The terms in such a series development explicitly represent the contributions due to $2, 3, \ldots, \infty$ fold scattering.

3. The hemispherical cavity

The special case of the hemispherical cavity is especially simple because the boundary of the cast shadow area and of the visible area are *great circles* on the sphere. This much simplifies the regions of integration in the expressions for the BRDF. The case of the plane of incidence is especially simple since then the boundary of the orifice, of the cast shadow, and of the visible region have common intersections. We can immediately perform one integration and the required integrations become one–dimensional.

3.1. General solution

Notice that the contributions to the radiance of the remitted beam are due to two distinct regions of the surface of the cavity:
— the (directly) irradiated and visible area;
— the visible region of the cast shadow area.
However, it is often more convenient to conceptually distinguish the contributions due to
— the primary irradiance, single scattering. This contribution is remitted from the directly irradiated and visible surface;
— the diffuse radiance which is due to the visible surface (either directly illuminated or in shadow).
Here we use the latter method. We need merely to write down the integrals representing these contributions.

In order to find the BRDF (at the mega scale) we need to find the ratio of the radiance remitted into the direction **e** (due to surface elements at the macro scale) to the irradiance of the plane (at the megascale). (Nicodemus *et al* 1977) The latter is simply $H^{\perp}\mathbf{i}\cdot\mathbf{n}$. The former can be found in the following way: The radiant flux remitted by the cavity into a solid angle $\Delta\Omega$ into the direction **e** is $\pi r^2\Delta\Omega\,\mathbf{n}\cdot\mathbf{e}\langle N\rangle$, that is the étendue of the beam (area of the orifice times the solid angle times the obliquety factor) times the required radiance. The radiance can alternatively be computed as an integral over the visible area of the cavity. The integral is

$$\int_{\text{visible}} \mathbf{m}\cdot\mathbf{e}\,\Delta\Omega N(p)\,da_p, \tag{14}$$

under the integral sign we find the étendue (area of the infinitesimal surface element times solid angle, times obliquety factor) times the local radiance. Notice that the obliquety factor at the macro scale $\mathbf{m}\cdot\mathbf{e}$ (**m** the surface normal at the macro scale) differs from that at the mega scale! We see that

$$\langle N\rangle = \frac{1}{\pi r^2\mathbf{n}\cdot\mathbf{e}}\int_{\text{visible}} N(p)\,\mathbf{m}(p)\cdot\mathbf{e}\,da_p. \tag{15}$$

Thus we can simply find the BRDF through integration over the local (macro scale) radiance, which is again simply related (via the BRDF at the micro scale) to the local irradiance.

In order to be able to perform the necessary integrations we have to find the regions of integration. The required boundaries are the orifice of the cavity, the edge of the cast shadow, and the boundary of the visible region. The integrations are over spherical triangles. Simplest expressions are obtained in suitable chosen coordinate systems. We define a Cartesian system and a polar coordinate system:

Since the pitted surface is *isotropic* no generality is lost if we take the first surface vector **a** in the plane of incidence.

The Cartesian system (ξ, η, ζ) is adapted to the viewing and source geometries. We let the ζ–axis coincide with the direction of the outer (mega scale) surface normal **n**. The ξ–direction is chosen to lie in the plane of incidence, the direction of **a**. Finally, we let the η–axis coincide with the **b**– direction, thus $\mathbf{e}_\xi \times \mathbf{e}_\eta = \mathbf{e}_\zeta$.

The polar system (ϑ, φ) is related to the (ξ, η, ζ)–system in the following way:

$$\xi = \sin\vartheta\cos\varphi \tag{16}$$

$$\eta = -\cos\vartheta \tag{17}$$

$$\zeta = \sin\vartheta\sin\varphi \tag{18}$$

Thus the vector **b** is the "south pole" of the spherical coordinates. The plane of the orifice of the cavity coincides with the plane $\varphi = 0$ or π, $0 \le \vartheta \le \pi$. Thus the surface of the cavity is the azimuth range $0 \le \varphi \le \pi$.

We represent the incident beam as $\mathbf{i} = (\sin\alpha, 0, \cos\alpha)$, and the viewing direction as $\mathbf{e} = (\sin\beta\cos\varepsilon, \sin\beta\sin\varepsilon, \cos\beta)$. Thus α is the co–elevation of the source and β the co–elevation of the eye. The azimuth of the viewing direction is ε. The primary irradiance is $H^{\perp}\sin\vartheta\sin(\alpha-\varphi)$. The expression for the obliquety factor is more complicated, it is:

$$\mu = \sin\vartheta(\cos\beta\sin\varphi - \cos\varepsilon\cos\varphi\sin\beta) - \cos\vartheta\sin\beta\sin\varepsilon. \tag{19}$$

The integration boundaries for the cavity itself and the irradiated region become simply φ–limits. The region of the visible area is also specified via the function $\vartheta_{\text{limit}}(\varphi)$. It is not hard to find an explicit expression from elementary geometry:

$$\vartheta_{\text{limit}} = \arctan \frac{\sin 2\beta \sin \varepsilon}{\cos 2\beta \sin \varphi - \cos \varepsilon \cos \varphi \sin 2\beta} \tag{20}$$

The integration over ϑ can immediately be carried out and we end up with the result:

$$\begin{aligned}
&\text{BRDF} = \\
&\frac{\varrho}{\pi^2 \cos\alpha \cos\beta} (\\
&\qquad \sin\beta \sin\varepsilon \int \sin(\alpha - \varphi)\, f_1(\vartheta_{\text{limit}}(\varphi))\, d\varphi \quad + \\
&\qquad \sin\beta \cos\varepsilon \int \cos\varphi\, f_2(\vartheta_{\text{limit}}(\varphi))\, d\varphi \quad + \\
&\qquad \cos\beta \int \sin(\alpha - \varphi) \sin\varphi\, f_2(\vartheta_{\text{limit}}(\varphi))\, d\varphi \\
&\quad) \quad + \\
&\frac{\varrho^2}{2\pi^2(2-\varrho)\cos\beta} (\\
&\qquad -\sin\beta \sin\varepsilon \int f_3(\vartheta_{\text{limit}}(\varphi))\, d\varphi \quad + \\
&\qquad \sin\beta \cos\varepsilon \int \cos\varphi\, f_4(\vartheta_{\text{limit}}(\varphi))\, d\varphi \quad + \\
&\qquad \cos\beta \int \sin\varphi\, f_4(\vartheta_{\text{limit}}(\varphi))\, d\varphi \\
&\quad)
\end{aligned} \tag{21}$$

where the first term (the contribution due to direct illumination and single scattering) is over the visible and illuminated area and the second term (the contribution due to multiple scattering) over the visible region. We have introduced the auxiliary functions

$$f_1(\vartheta) = -\frac{1}{3} \sin^3 \vartheta \tag{22}$$

$$f_2(\vartheta) = \tfrac{2}{3} + \tfrac{3}{4} \cos\vartheta - \tfrac{1}{12} \cos^3\vartheta + \tfrac{1}{4} \cos\vartheta \sin^2\vartheta \tag{23}$$

$$f_3(\vartheta) = -\frac{1}{2} + \frac{1}{2} \cos^2 \vartheta \tag{24}$$

$$f_4(\vartheta) = \frac{\pi}{2} - \frac{\vartheta}{2} + \frac{1}{2} \cos\vartheta \sin\vartheta \tag{25}$$

for convenience.

We have not been able to do the integrals in terms of elementary functions (notice that the integrands are nasty: One has to substitute ϑ_{limit} (equation 20) into the f_i (equations 22–25) and these again in the integral formulations of equations 21). However, it is easy enough to evaluate the integrals to any required level of precision (in radiometry these requirements tend to be rather modest anyway, however, this is not an issue). Thus we are able to find the BRDF for arbitrary spherical cavities *exactly* (that is to say: taking the effects of vignetting, cast shadow, interposition and interreflection exactly into account).

3.2. Analytical relations for the plane of incidence

It is an easy exercise to express the general result in terms of elementary functions when we limit the investigation to visual directions in the plane of incidence, that is to say, $\varepsilon = 0$ or π. This is more of a physicist's delight than anything else, however, at times it may be convenient to have analytical expressions even though these are not particularly simple. It is convenient to let the sign of β reflect forward, or backward scattering, *i.e.*, we reckon β positive when $\epsilon = 0$ and negative when $\epsilon = \pi$.

The results are best expressed in terms of the auxiliary functions A, B, C, D:

$$A = \frac{2\varrho \cos(\alpha - |\beta|)}{3\pi^2 \cos\alpha \cos|\beta|} (\pi - 2\alpha + \sin 2\alpha) \tag{26}$$

$$B = \frac{2\varrho \cos(\alpha - |\beta|)}{3\pi^2 \cos\alpha \cos|\beta|} (\pi - 2|\beta| + \sin 2|\beta|) \tag{27}$$

$$C = \frac{2\varrho \cos(\alpha + |\beta|)}{3\pi^2 \cos\alpha \cos|\beta|} (\pi - 2\alpha - 2|\beta| + \sin 2\alpha + \sin 2|\beta|) \tag{28}$$

$$D = \frac{\varrho^2}{2\pi(2-\varrho)} \tag{29}$$

In terms of these expressions the BRDF is:
— in the case of forward scattering, illuminated part visible ($\alpha + \beta < \pi/2$): C+D;
— in the case of forward scattering, only shadow part visible ($\alpha + \beta > \pi/2$): D;
— in the case of backward scattering, illuminated part visible ($\beta < \alpha$): A+D;
— in the case of backward scattering, only shadow part visible ($\beta > \alpha$): B+D;
The contribution D describes the multiply scattered radiation.

3.2.1. Relations in the plane of incidence BRDF's for the plane of incidence are presented in figure 4 and remitted radiances in figure 5. These results have been calculated for a white ($\varrho = 1$) surface. The pitted surface is typically lighter than a Lambertian surface except for views in the oblique forward scattering region. It is *much* lighter in the backscatter direction. This is intuitively obvious, because in the backscatter condition an appreciable fraction of the surface is effectively illuminated and viewed from the *normal* di-

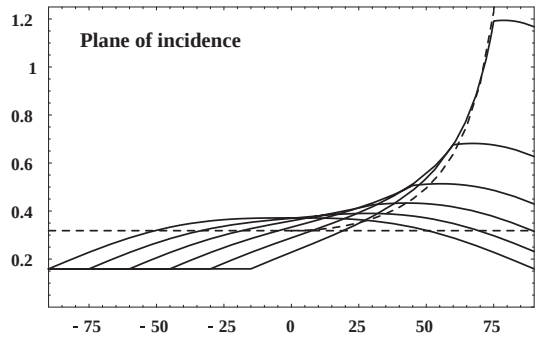

Fig. 4. BRDF's for viewing directions in the plane of incidence. The co–elevation of the source is 0° through 75° in steps of 15°. The co–elevation of the viewing direction (horizontal axis) is negative in the forward, positive in the backward scattering region. The horizontal dashed line denotes the Lambertian BRDF. The dashed curve going off to infinity for the backward scattering denotes the theoretical maximum due to the attitude effect.

rection. Intuitively, such an effect would be maximal for a one–dimensional "saw tooth surface" (figure 6) with surface strips along and orthogonal to the incident beam where the "boost" with respect to the Lambertian surface could be as high as $1/\mathbf{i}\cdot\mathbf{n}$. We may call this the "attitude effect": For a rough surface a large percentage of the surface may receive normal irradiance on the macro scale, even for oblique incidence on the mega scale. It can be seen that the boost yielded by the pitted surface is indeed close to the theoretical maximum. For rather normal incidence it is even higher due to the effect of interreflection. In the oblique forward scattering region one sees almost only the multiply scattered radiation.

Notice that the qualitative shape of the curves in figure 4 is well captured via the following two asymptotic limits: For extreme forward scattering the diffuse flux dominates and the BRDF is half that of the Lambertian BRDF. For shallower cavities this factor will be less than one half: It follows immediately from the expression for the diffuse radiance. (In the limit for almost flat cavities the diffuse contribution tends to zero, but the directions for which only the diffuse contribution can be seen crowd near grazing incidence.) For backward scattering the attitude effect dominates the BRDF. For shallower cavities the attitude effect will be less effective because the required surface orientations are lacking.

From the radiance plots (figure 5) we see that the radiance in the forward scattering direction is roughly independent of the direction of the incident beam: The

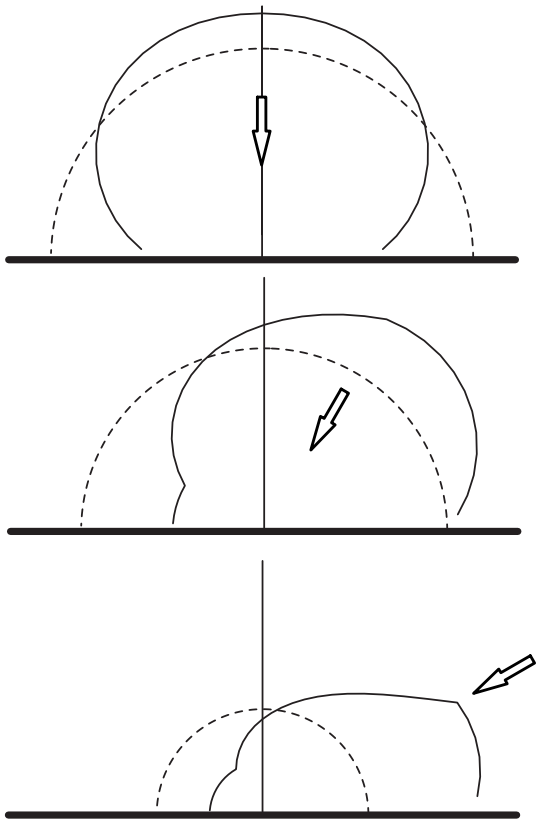

Fig. 5. Polar plot of the remitted radiance for various directions of the incident beam, all in the plane of incidence. The dashed circle represents the radiance for a Lambertian surface of the same albedo (at the micro scale). Notice the radiance "boost" and the strong back scattering. The back scattering increases as the incident beam impinges on the surface more obliquely.

surface roughly behaves as a normally irradiated Lambertian surface. The diffuse component in the forward scattering direction behaves like due to a Lambertian surface of albedo 0.5. In this case the value of the BRDF is simply

$$BRDF_{\text{forward}} = \frac{\varrho^2}{2\pi(2-\varrho)}, \tag{30}$$

or, approximately,

$$\frac{1}{4\pi}(\varrho^2 + \frac{\varrho^3}{2} + \frac{\varrho^4}{4} + \frac{\varrho^5}{8} + \frac{\varrho^6}{16} + \frac{\varrho^7}{32} + O(\varrho^8)). \tag{31}$$

Notice that this is a very nonlinear relation (see figure 7). When the material is somewhat colored (ϱ a function of the wavelength), the remission spectrum from the pit will thus differ markedly from that of the plane: The remitted beam suffers a *color shift*. The effect is to boost high albedo, thus a yellowish mate-

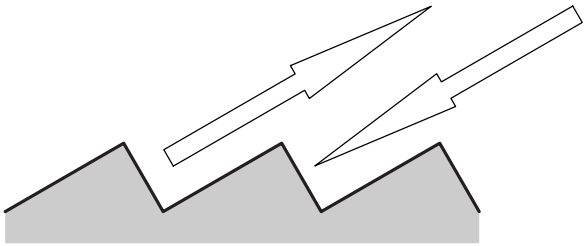

Fig. 6. A "sawtooth" surface "tuned" to a backscattering direction of 60°. Notice that for the indicated directions of the incident and remitted beams the surface behaves like a Lambertian surface at normal incidence.

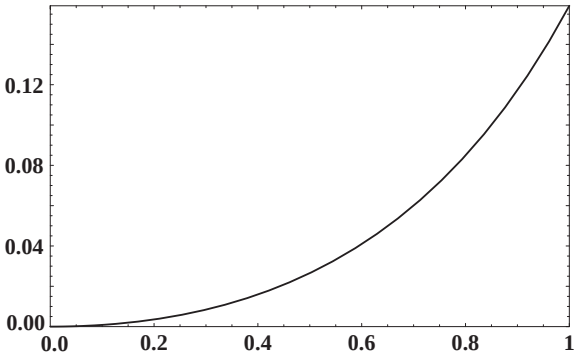

Fig. 7. The diffuse BRDF (forward scattering) as a function of the albedo of the substrate. Notice the nonlinear relation favouring the high albedo's.

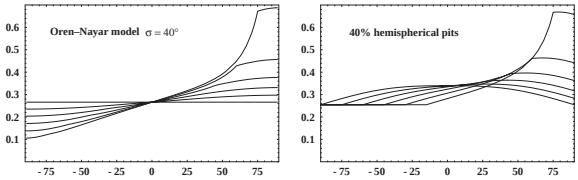

Fig. 8. On the left the BRDF according to the model of Oren and Nayar ($\varrho = 1$), and on the right the BRDF for a surface that is for 40% covered with hemispherical pits ($\varrho = 1$). (On the horizontal axis the viewing direction, parameter is the direction of incidence.)

rial (ϱ increases with increasing wavelength) will become more reddish. Such effects have been observed by painters (*e.g.*, the French academic school): In the human nude one often sees the navel treated as a uniform reddish blotch. The uniformity is due to the interreflection (no gradients due to shading) and the reddish color to the nonlinearity mentioned above.

In figure 8 we present a comparison with the V–groove model of Oren and Nayar (Nayar and Oren 1995, Oren and Nayar 1995). For the Oren–Nayar model (left) we set an albedo of unity (perfectly white substrate) and σ (roughness parameter) of 40°. The figure on the right is for a white substrate for 40%

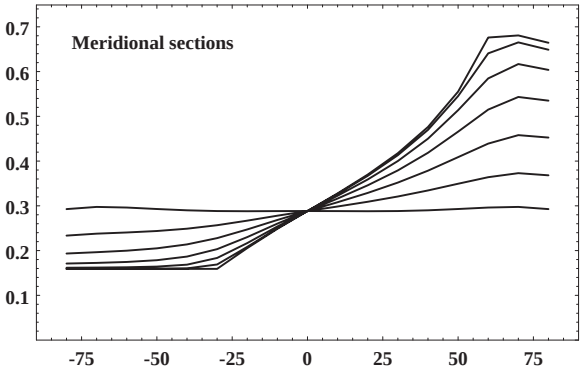

Fig. 9. BRDF's for the hemispherical cavity and for various meridional sections ranging from the plane of incidence to orthogonally to it. The co–elevation of the source is 60°. (Viewing direction along the horizontal axis, parameter is the azimuth.)

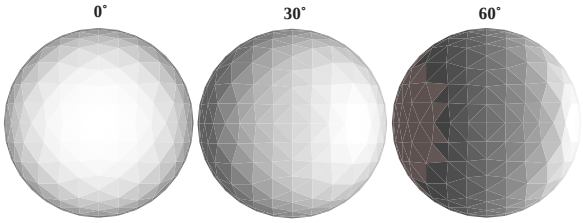

Fig. 10. Plots of the remitted radiance for the hemispherical cavity and for directions of incidence of 0° (left), 30° (middle) and 60° (right). The backscatter direction is towards the right, the plane of incidence is the horizontal cross section.

covered with hemispherical pits. It is probably possible to obtain a better fit by selecting some distribution of apertures. We didn't bother because it will already be difficult to distinguish on the basis of actual measurements. Clearly the predictions of these (geometrically quite dissimilar) models are very similar. This is of course to be expected since the physical processes that cause the deviations from the Lambertian BRDF are the same and depend only little on the *precise* geometry. The result thus also demonstrates that such ideal models of rough surfaces will be applicable to a rather wide range of actual surface geometries.

These relations appear to be in reasonable agreement with the empirical results obtained by van Diggelen (1959). The major difference is that the effect of interreflections seems to be absent in van Diggelen's result, even for the case of the white (magnesium oxide coated) surface. This is hard to explain since the effect easily exceeds the instrumental tolerances. Indeed, the effect is immediately obvious visually in an informal set up. The strong backscattering is a dominant feature in van Diggelen's results. In the theoretical lunation curves the backscatter peak is strongly under-

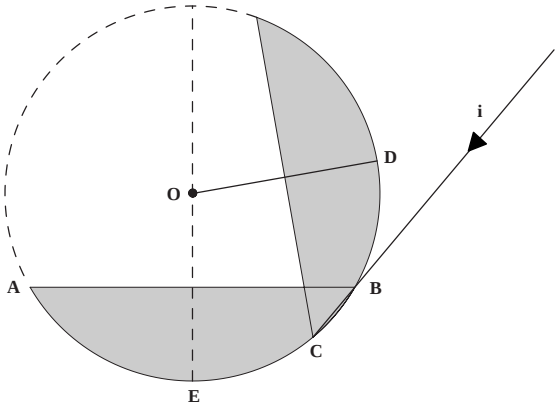

Fig. 11. Geometry of vignetting in the case of the shallow pit. The surface of the cavity is the arc AEB. Only the part CB of the edge of the cast shadow falls into the cavity. The pole of the small circle that is the cast shadow area is D. This small circle has the same radius as the orifice of the cavity. Seen from the deepest point of the pit (E) it lies in the direction of the incident beam: This makes it very easy to calculate the pole D. Given D it is a simple matter to find whether any point of the cavity is in shadow: Simply check the projection of its radius vector on OD.

estimated, no doubt because of the irrealistic neglect of the attitude effect.

3.2.2 Relations outside of the plane of incidence In figure 9 we show meridional sections for planes outside of the plane of incidence. Both the boost due to the attitude effect and the effect of cast shadow and interreflection become much less conspicuous: For a section at right angles to the plane of incidence we find that the BRDF almost coincides with the Lambertian case.

In figure 10 we illustrate the distribution of the remitted radiance in a more graphical manner. (These figures have been calculated with the method discussed in the next section.) One sees that the boost due to the attitude effect is largely confined to the backward scattering direction, both in elevation and in azimuth.

4. The shallow pit

The case of the shallow cavity ($\Psi < \pi/2$) is not much more complicated than that of the hemispherical cavity *in principle*. However, the boundary of the region of integration is more involved (spherical triangular and biangular regions bounded by small circular arcs), so the expressions (even without evaluation of the integrals) are complicated. In this case any expression in terms of elementary functions (even if it proves possible) would almost certainly be so complicated as to be practically worthless. Even the expression involving unevaluated definite integrals is less useful than in the hemispherical case because numerical evaluation of these integrals (given the unpleasant boundaries) is bound to be a slow process. In this case it is much more convenient to solve the integrals numerically via Monte Carlo methods. Since arbitrarily close approximation of the exact numerical values is guaranteed (because an exactly stated problem is being solved via statistical sampling) such a solution is—from a pragmatic point of view—as good as any.

4.1. Numerical calculation of the radiance for an elementary beam

A simple method uses the following algorithm:

Firstly, we provide methods that allow us to find the point on the surface of the cavity that corresponds to a given viewing direction and a certain position inside the planar disk of the orifice of the concavity. *Secondly*, we provide a method that allows us to decide whether any point on the surface of the cavity is located in the region of the cast shadow. *Thirdly*, we provide a method to find the irradiance for any point on the surface of the cavity: This allows us to specify the radiance of the remitted beam from that location. (See figure 11.)

One easily checks that all three methods are essentially trivial. Given these we are in a position to find the radiance for any point in the planar disk of the orifice. When we sample the projection of the planar disk of the orifice on a plane orthogonal to the viewing direction uniformly, we can find the average radiance immediately and thus obtain the BRDF. (See figure 12.) Because we have also obtained the radiance distribution this method also yields the radiance histogram and the spatial structure of the "texton" corresponding to a single cavity. By repeating such textons according to the distribution of pits we find the *texture* of the pitted surface as a function of source and viewing geometries.

This is a practical method that (in the case of the hemispherical cavity off the plane of incidence) is almost as fast as the numerical integration. It is much faster than simulation via (exact) ray tracing or radiosity calculations because the interreflection problem has already been solved exactly.

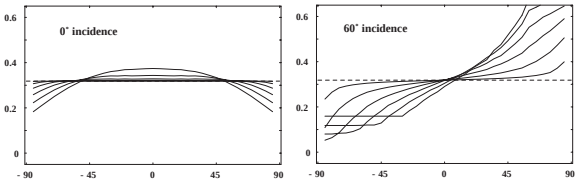

Fig. 12. Effect of variation of the aperture Ψ on the BRDF. We illustrate apertures of 15°, 30°, 45°, 60°, 75° and 90°. On the left normal incidence, on the right 60° incidence. Both graphs represent the BRDF in the plane of incidence. Notice that the BRDF's for the shallow pits are in between those for the hemispherical pit and the Lambertian surface. However, they are not linear combinations (like a Lambertian plane sparsely covered with hemispherical pits). For the shallow pits the shadow geometry is different from that of the hemispherical pit and interreflection plays a lesser role. (Viewing direction along the horizontal axis, parameter is the aperture.)

4.2. Textons and radiance histograms

In figure 13 we illustrate views of the cavity for various source and viewing geometries. These examples have been computed for the case of the hemispherical cavity in order to make it convenient to relate these pictures to the BRDF results discussed above. Of course the method allows us to obtain such results for pits of arbitrary apertures. In figure 14 we present radiance histograms for these same cases.

The lay out of figure 13 is as follows: Each subpanel is a picture of the surface from the viewing direction β (co–elevation), ε (azimuth) and direction of incidence α (co–elevation). The subpanels correspond to the triples $(\alpha, \beta, \varepsilon)$ (the value of ε is omitted when irrelevant):

$$
\begin{array}{ccc}
(0^\circ, 0^\circ) & (0^\circ, 30^\circ) & (0^\circ, 60^\circ) \\
 & (30^\circ, 30^\circ, 0^\circ) & (30^\circ, 60^\circ, 0^\circ) \\
(30^\circ, 0^\circ) & & \\
 & (30^\circ, 30^\circ, 180^\circ) & (30^\circ, 60^\circ, 180^\circ) \\
 & (60^\circ, 30^\circ, 0^\circ) & (60^\circ, 60^\circ, 0^\circ) \\
(60^\circ, 0^\circ) & & \\
 & (60^\circ, 30^\circ, 180^\circ) & (60^\circ, 60^\circ, 180^\circ)
\end{array}
$$

For the case of normal incidence ($\alpha = 0^\circ$, top row in figures 13 and 14) the relations are easily understood intuitively. For normal viewing ($\beta = 0^\circ$) the texton shows a light center with a dark edge. This is largely due to the variation of surface attitudes: At the center the surface is normally illuminated, at the edge the (primary) irradiance vanishes.

Due to interreflections the center is actually lighter than the plane. The corresponding radiance histogram

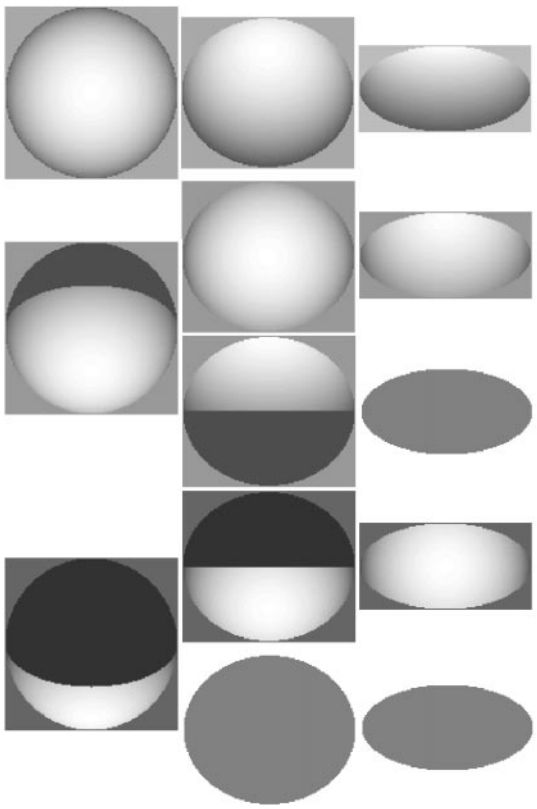

Fig. 13. "Textons" for the hemispherical pit, that are views of the pit for various viewing and source geometries. For illustrative purposes the maximum radiance is represented by the paper white in each picture. The lay out of the panel is explained in the text.

reflects the fact that the area covered with lighter pixels is relatively large compared to that for the darker pixels: In this case it is not hard to find an analytical expression for the histogram. As a result the histogram is strongly skewed towards the high radiance end.

Due to interreflections the radiance nowhere vanishes and the histogram starts at a finite radiance value (equal to the diffuse radiance). For oblique viewing ($\beta = 30^\circ$ and $\beta = 60^\circ$) effects of perspective change the texton and the histogram: This is indeed a purely perspective effect since the radiance (on the micro scale) doesn't depend on direction (the surface is Lambertian at the micro scale). As a result the histogram becomes less skewed (the oblique viewing works to the advantage of the dark parts and the disadvantage of the light parts), and at $\beta = 60^\circ$ is indeed more symmetric.

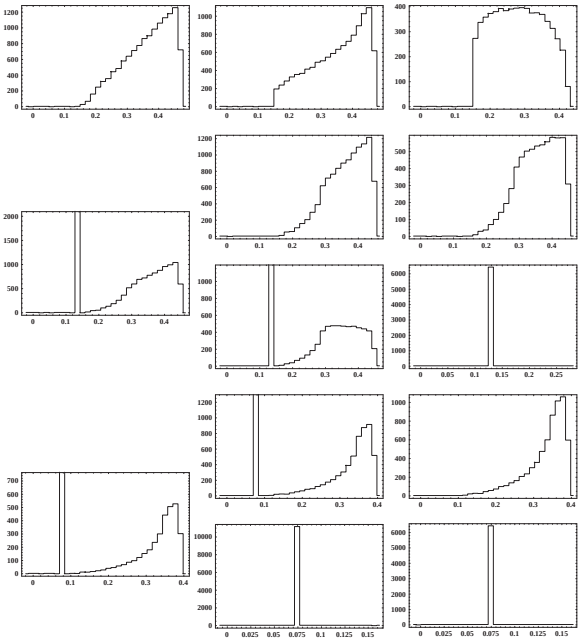

Fig. 14. Radiance histograms for the textons illustrated in figure 13. The lay out of figure 13 and 14 is identical.

For the case of somewhat oblique incidence ($\alpha = 30^\circ$, middle row(s) in figures 13 and 14) the effect of the cast shadow already becomes conspicuous. For normal viewing ($\beta = 0^\circ$) we see that the pattern from the previous case is somewhat shifted, whereas the cast shadow somewhat invades the cavity. In the histogram we still find the basic structure from normal viewing, but also an additional mode due to the shadow: Thus the histogram is bimodal. The mode due to the cast shadow is a narrow peak because the diffuse radiance is constant over the surface of the cavity. It is located exactly at the toe of the mode due to single scattering. For somewhat oblique viewing ($\beta = 30^\circ$) we see a dramatic difference between the forward and backward scattering conditions. In the backward scattering ($\varepsilon = 0^\circ$) condition both the textons and the histograms are rather similar to those of the case of normal incidence. Indeed, the cast shadow is not visible from this direction. However, for the forward scattering direction ($\varepsilon = 180^\circ$) the cast shadow completely changes the texton, which becomes a light–dark dipole pattern, and the histogram is strongly bimodal. For even more oblique viewing ($\beta = 60^\circ$) in the forward scattering condition the (directly) irradiated area is not visible, thus the texton has degenerated to a dark blob, and the histogram contains only the narrow mode due to multiple scattering. Notice that the mode is located at a finite radiance, thus the texton is not a *black* blob, but is grayish.

For the case of very oblique incidence($\alpha = 60^\circ$, lowest row(s) in figures 13 and 14) the cast shadow dominates the view, even in the case of normal viewing ($\beta = 0^\circ$). The histogram is strongly bimodal and due to both perspective and photometric effects the shape of the single scattering mode is somewhat different from the case of normal incidence discussed above. For the backward scattering direction ($\varepsilon = 0^\circ$) we see that only the single scattering peak remains for very oblique viewing ($\beta = 60^\circ$). The texton is almost uniformly light and *much* lighter than the plane (compare the case of normal incidence!), clearly showing the boost due to the attitude effect. For the forward scattering direction ($\varepsilon = 180^\circ$) both the texton and the histogram are dominated by the cast shadow and the interreflection. The cavity shows up as a uniform grayish blob and the histogram is unimodal with a very narrow peak.

This general behavior (textons similar to light blobs with dark border, light–dark dipole and uniform dark blobs, unimodal and bimodal histograms with narrow multiple scattering mode at low radiances and broad single scattering modes (shape much dependent on geometry of the cavity and viewing perspective) at high radiance) can be retraced in measurements of many natural materials. Close study of the changes in the modal structure of the histogram may be expected to be useful in remote sensing applications. (Richards 1982 has a rather interesting discussion. Although his model is quite different from the present one the predicted histograms are similar. His data on the histogram of foliage is remarkably like the histogram for a pitted surface.) The dipole structure of textons is an immediate cue to the source direction and is likely to be so used in human visual perception.

Notice how the textons change dramatically with both the source and the viewing geometry. This illustrates the fact that the commonly used technique of "texture mapping" in computer graphics (Foley *et al* 1990) can only yield results that are far off the mark. Texture mapping works only for a given source and viewing geometry, but that evidently defeats its very purpose.

4.2.1. Illustrative example: Rough plaster Because the generic physical phenomena are essentially the same for all rough surfaces that are approximately Lambertian on a microscale (vignetting, interreflec-

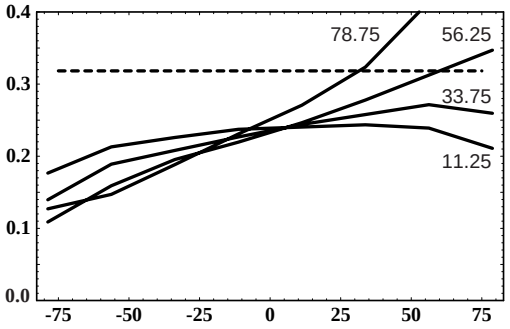

Fig. 15. BRDF's for sample no. 11 from the database (rough plaster) for viewing and incident directions in the plane of incidence. (Along the horizontal axis the viewing direction, parameter is the direction of incidence.)

tion, shadowing and the attitude effect), one may infer that the pattern identified above (rather roughly of course) will predict the qualitative behavior. (A more precise description would involve a number of parameters characterizing the nature of the relief and the exact surface properties.) This turns out to be the case, in the CURET database (Columbia and Utrecht universities `http://www.cs.columbia.edu/CAVE/curet/`, see Dana *et al.* 1996 and 1997) most surfaces in this general category seem to fit the pattern, at least qualitatively. As an example we pick sample #11 ("rough plaster"). We limit the discussion to the plane of incidence. Co–elevations available in the data base are $\pm 11.25^\circ$, $\pm 33.75^\circ$, $\pm 56.25^\circ$ and $\pm 78.75^\circ$. Since the camera and the source could not be on the same direction some combinations are not available though. In total we have 28 combinations.

The BRDF (figure 15) is probably most insensitive with respect to the precise parameters since it is merely an overall measure and indeed is seen to fit the pattern quite well: Apparently the surface is not unlike a somewhat greyish surface pitted with shallow spherical concavities. The texture images (figure 16) show most of the generic effects though perhaps the effects of interreflection are not evident due to the low albedo and shallowness of the concavities. The texture images indeed change dramatically with both the source and the viewing geometry. In the histograms (figure 17) we notice the expected modes and their expected shifts with changes of directions, though it is hard to evaluate the shape and strength of the modes precisely. At least the qualitative pattern is the expected one for a surface covered with shallow pits. The major exception (though it is a small effect) is a *third* mode at the high radiances. This mode is apparently due to surface features that stick out and catch light where the ideal pitted surface would be dark, so much can be gleaned from the texture images.

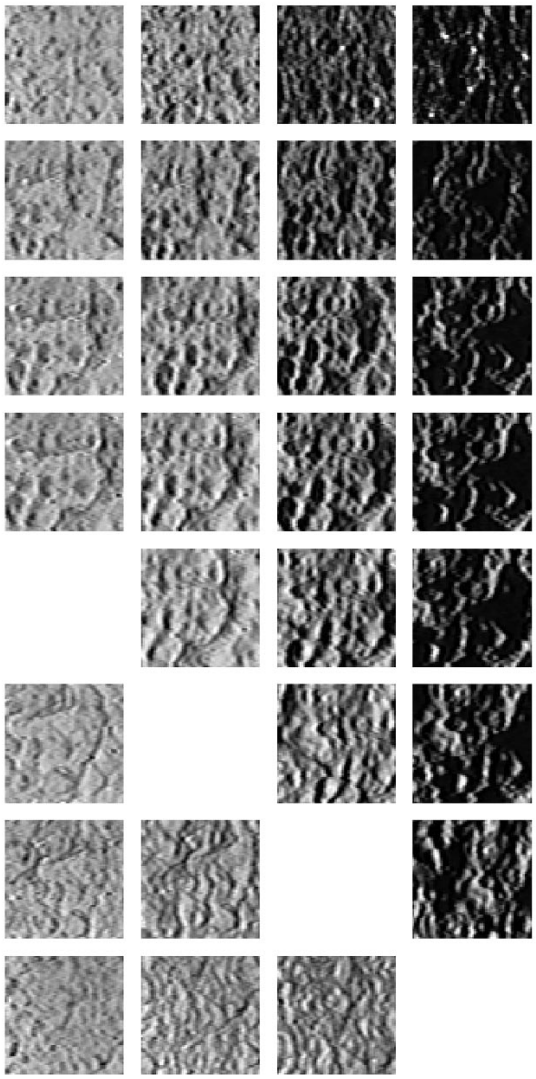

Fig. 16. Textures for sample no. 11 from the database (rough plaster) for viewing and incident directions in the plane of incidence. The layout is the same as in the next figure (figure 17).

5. Conclusion

The problem of finding the BRDF for a rough surface is much simplified when the various global geometrical and radiometrical effects are confined to finite regions.

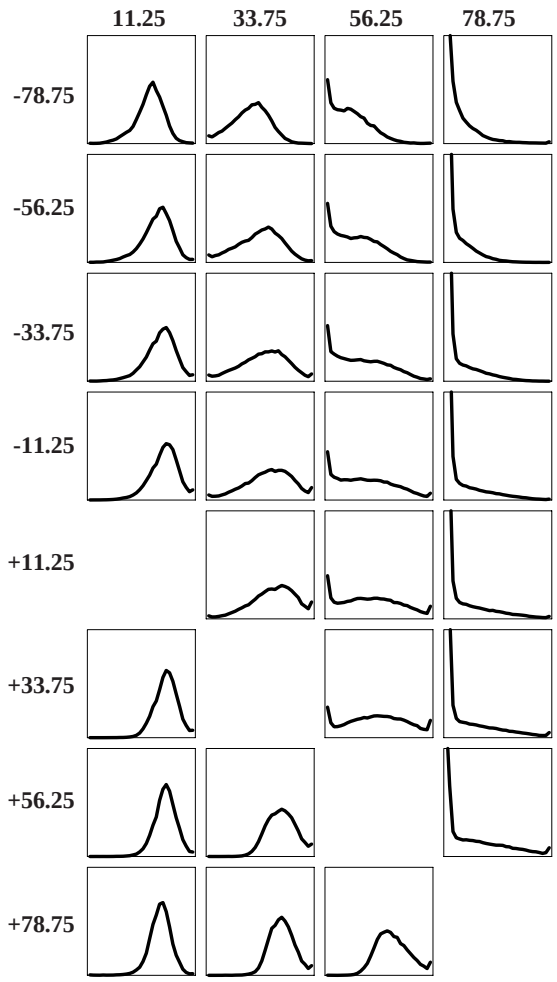

Fig. 17. Histograms for sample no. 11 from the database (rough plaster) for viewing and incident directions in the plane of incidence. The angles of incidence are indicated over the top row, the viewing angles at the left of the first column.

This limits the viable models to "pitted surfaces", *i.e.*, distributions of concavities in the plane. The global effects are then confined to the concavities and there can be no "cross talk" between remote parts of the surface. Examples are the V–groove surface (the Oren–Nayar model) and the model of spherical pits investigated in this paper.

The analysis is much simplified when both the vignetting and the interreflection problems are tractable. The vignetting problem involves global geometry. It is especially simple for the V–grooves and proves to be reasonably simple for the case of spherical concavities. The interreflection problem involves the solution of a Fredholm integral equation. The kernel is the mutual étendue for any two infinitesimal surface elements of the cavity. Here the spherical pit model is singularly trivial because the kernel is a constant. Thus the integral equation can be reduced to an algebraic one.

The spherical concavities can be used to form a variety of "thoroughly pitted surfaces". The free parameters are:
— the albedo on the micro scale;
— the distribution of apertures;
— the distribution of diameters;
— the fraction of the surface area covered with pits.
The fraction of the surface area covered with pits may vary from very little (cheese with a few holes) to almost unity (sliced bread, pumice stone). The distribution of apertures makes it possible to construct BRDF's that are linear combinations (weighed averages) of the BRDF's for pits of various diameter–depth ratios. The distribution of diameters has no effect on the BRDF: It affects only the texture. The albedo (on the micro scale) of course affects the overall albedo (scaling of the BRDF), but it also affects the *shape* of the BRDF because it affects the influence of the interreflections. These degrees of freedom make it possible to represent a wide class of rough surfaces. It may be expected that the BRDF may be well represented, the histogram of radiance values at least semi– quantitatively well, and the texture to some extent, mainly in a qualitative sense (because most actual surfaces will fail to be *truly* pitted surfaces in the ideal sense). (Stavridi *et al* 1997.)

Notice that the pitted surface model can be adapted to represent a large class of textures since there is complete freedom in the statistical distribution of orifice diameters and apertures and also in the geometrical configuration in which the pits are placed.

The advantage of the present model is that it yields *exact* results for a type of surface that is both reasonable and geometrically possible (the V–grooves model fails on this issue). Thus it is especially useful from a conceptual point of view. The fact that it also yields histograms and texture maps makes it especially attractive. From a pragmatic point of view one often wants a simple expression for the BRDF of rough surfaces with some natural degrees of freedom. Here both the present model and the V–grooves model work OK. In many cases it will be preferable to use (analytically much simpler and faster to compute) developments of these expressions in terms of a truncated series of scattering modes (Koenderink *et al* 1996). The fact that such expressions have been obtained from exact mod-

els gives them some additional credibility, but that is not the main point.

References

Beckmann, P. and Spizzichino, A. 1963. *The scattering of electromagnetic waves from rough surfaces*. New York: Pergamon.

Beckmann, P. 1965. Shadowing of random rough surfaces. *IEEE Transactions on Antennas and Propagation*, AP–13: 384–388.

Blinn, J. F. 1977. Models of light reflection from computer synthesized pictures. *ACM Computer Graphics (SIGGRAPH77)*, 19(10): 542– 547.

Born, M. and Wolf, E. 1980. *Principles of Optics*, 6th ed. Oxford: Pergamon.

Buckley, H. 1927. On the radiation from the inside of a circular cylinder. *Philosophical Magazine*, 4: 753–757.

Buhl, D., Welch, W. J., and Rea, D. G. 1968. Reradiation and thermal emission from illuminated craters on the lunar surface. *Journal of Geophysics Research*, 73: 5281–5295.

Dana, K. J., Van Ginneken, B., Nayar, S. K., and Koenderink, J. J. 1996. Reflectance and texture of real–world surfaces. *Columbia University Technical Report* CUCS–048–96.

Dana, K. J., Van Ginneken, B., Nayar, S. K., and Koenderink, J. J. 1997. Reflectance and texture of real–world surfaces. *Proc.IEEE Conf. on Comp.Vision and Patt.Rec. (CVPR)*.

Diggelen, van J. 1959. Photometric properties of lunar crater floors. *Recherches Observatoire Utrecht*, 14: 1–114.

Fock, V. 1924. Zur Berechnung der Beleuchtungsstärke. *Zeitschrift für Physik*, 28: 102–113.

Foley, J. D., van Dam, A., Feiner, S. K., and Hughes, J. F. 1990. *Computer Graphics, Principles and Practice*, 2nd ed. Reading, Mass.: Addison–Wesley.

Gershun, A. 1939. The light field. Transl. P. Moon and G. Timoshenko. *Journal of Mathematical Physics*, 18: 51.

Gibson, J. J. 1950. *The perception of the visual world*. Boston: Houghton–Mifflin.

Hunter, R. S. 1975. *The measurement of appearance*. New York: Wiley.

Jacquez, J. A. and Kuppenheim, H. F. 1955. Theory of the integrating sphere. *Journal of the Optical Society of America*, 45: 460–470.

Kerker, M. 1969. *The scattering of light and other electromagnetic radiation*. New York: Academic Press.

Koenderink, J. J. and van Doorn, A. J. 1983. Geometrical modes as a general method to treat diffuse interreflections in radiometry. *Journal of the Optical Society of America*, 73: 843–850.

Koenderink, J. J., van Doorn, A. J., and Stavridi, M. 1996. Bidirectional Reflection Distribution Function expressed in terms of surface scattering modes. *Computer Vision–ECCV'96*, B. Buxton and R. Cipolla (Eds.), Vol II, Springer: Berlin.

Koenderink, J. J. and van Doorn, A. J. 1996. Illuminance texture due to surface mesostructure. *Journal of the Optical Society of America*, A13: 452–463.

Kortüm, G. 1969. *Reflectance spectroscopy*. New York: Springer.

Lambert, J. H. 1760. *Photometria sive de mensura de gradibus luminis, colorum et umbræ*. Augsburg: Eberhart Klett.

Longhurst, R. S. 1957. *Geometrical and physical optics*. London: Longmans, Green and Co.

Minnaert, M. 1941. The reciprocity principle in lunar photometry. *Astrophysical Journal*, 93: 403–410.

Moon, P. 1940. On interreflections. *Journal of the Optical Society of America*, 30: 195–205.

Moon, P. and Spencer, D. E. 1981. *The photic field*. Cambridge, Mass.: The M.I.T. Press.

Nayar, S. K., Ikeuchi, K., and Kanade, T. 1991. Surface reflection: physical and geometrical perspectives. *IEEE Transactions on Pattern Recognition and Machine Intelligence*, 13: 611–634.

Nayar, S. K. and Oren, M. 1995. Visual appearance of matte surfaces. *Science*, 267: 1153–1156.

Nicodemus, F. E., Richmond, J. C., Hsia, J. J., Ginsberg, I. W., and Limperis, T. 1977. *Geometrical considerations and nomenclature for reflectance*. National Bureau of Standards (U.S.), Monograph 160.

Öpik, E. 1924. Photometric measures of the moon and the earth–shine. *Publ. de L'Observ. Astron. de L'Univ. de Tartu*, 26: 1–68.

Oren, M. and Nayar, S. K. 1995. Generalization of the Lambertian model and implications for machine vision. *International Journal of Computer Vision*, 14: 227–251.

Richards, W. A. 1982. Lightness scale from image intensity distributions. *Applied Optics*, 21: 2569–2582.

Smith, B. J. 1967. Geometric shadowing of a random rough surface. *IEEE Transactions on Antennas and Propagation*, AP–15: 668–671.

Stavridi, M., van Ginneken, B., and Koenderink, J. J. 1997. Surface bidirectional reflection distribution function and the texture of bricks and tiles. *Applied Optics*, 36: 3717–3725.

Torrance, K. E. and Sparrow, E. M. 1967. Theory for off–specular reflections from roughened surfaces. *Journal of the Optical Society of America*, 57: 1105–1114.

Wagner, R. J. 1967. Shadowing of randomly rough surfaces. *Journal of the Acoustical Society of America*, 41: 138–147.